ELSEVIER

International Journal of Mass Spectrometry 185/186/187 (1999) 413–424

International Journal of Mass Spectrometry

Experimental and theoretical investigation into the structural and thermodynamic properties of the mixed methyl halide association radical cations

Linda S. Nichols, Andreas J. Illies*

Department of Chemistry, Auburn University, Auburn, AL 36849-5312, USA

Received 5 June 1998; accepted 20 August 1998

Abstract

An experimental and theoretical study of the ion/molecule association reactions of methyl halide radical cations with mixed methyl halides (X, Y = I, Br, Cl, F) has been carried out. MS/MS unimolecular and collision-induced dissociation experiments were performed on the association products and provide strong evidence for formation of a two-center three-electron (2*c*-3*e*) bonded structure, $[CH_3X\cdot\!\cdot YCH_3]^{\cdot +}$, for all association products excluding $[C_2H_6FCl]^{\cdot +}$. The $[C_2H_6FCl]^{\cdot +}$ results suggest the following atomic connectivity for this association product: $[CH_2Cl–H–FCH_3]^{\cdot +}$. Two metastable fragmentation pathways were observed for $[CH_3I\cdot\!\cdot BrCH_3]^{\cdot +}$ and $[CH_3Br\cdot\!\cdot ClCH_3]^{\cdot +}$: direct cleavage of the 2*c*-3*e* bond and elimination of a methyl group. Only direct cleavage was observed in $[CH_3I\cdot\!\cdot ClCH_3]^{\cdot +}$, $[CH_3I\cdot\!\cdot FCH_3]^{\cdot +}$, and $[CH_3Br\cdot\!\cdot FCH_3]^{\cdot +}$. Kinetic energy release distributions were measured and unimolecular kinetic modeling studies were performed on the metastable reaction pathways. Unimolecular kinetic modeling was carried out using phase space calculations and molecular parameters from density functional theory (DFT) calculations. DFT was also used to investigate the potential energy surfaces for each system. (Int J Mass Spectrom 185/186/187 (1999) 413–424) © 1999 Elsevier Science B.V.

Keywords: 2*c*-3*e* bonding; Ion/molecule reactions; MS/MS; Kinetic energy release; Methyl halides

1. Introduction

Although many methyl halide systems containing two-center three-electron (2*c*-3*e*) bonds have been identified both in theoretical [1–4] and experimental investigations [1,2,5–7], little information exists on this bonding in the gas-phase [1,2,8,9]. Our group has long been interested in 2*c*-3*e* bonding in gas-phase ion/molecule reaction mechanisms and association products. Symmetric 2*c*-3*e* bonding between methyl halides has been the subject of studies by our group [2] and others [1]. Here, we present the formation of unsymmetric 2*c*-3*e* bonds between methyl halides in the gas-phase.

2*c*-3*e* Bonding was first postulated by Linus Pauling in 1931 [10]. A molecular orbital (MO) diagram illustrating symmetric 2*c*-3*e* bonding is shown in Scheme 1. The simple MO diagram predicts that, since the bond order is one-half, the 2*c*-3*e* bond should have a bond energy that is approximately one-half that of a normal 2*c*-2*e* bond. The 2*c*-3*e* bond length should also be longer than a correspond-

* Corresponding author.

Dedicated to Professor Michael T. Bowers on the occasion of his 60th birthday.

PII S1387-3806(98)14171-4

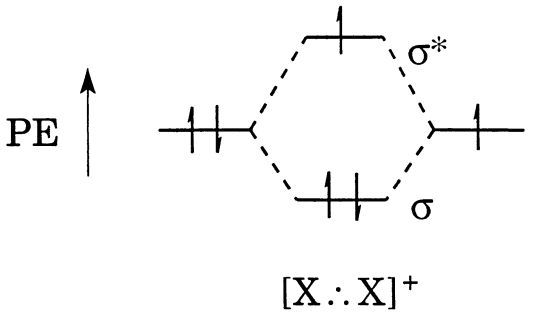

Scheme 1.

ing 2*c*-2*e* bond. However, the destabilizing effect of an electron in the antibonding σ^* orbital is greater relative to the stabilizing effect of the two bonding σ electrons and a bond order of less than 0.5 results [11]. These predictions have proved to be correct in prior studies of 2*c*-3*e* X.∴X (X = I, Br, Cl, F) and S.∴S bonds [1,2,9].

In the mixed methyl halide systems, the two reacting species have different ionization energies (IEs) and their interaction gives rise to the MO diagram in Scheme 2. Due to their different IEs, the interacting MOs have different energies resulting in a weaker 2*c*-3*e* bond than if the energies were equal. It has been observed that the energies of the interacting moieties must be close in order for a stable 2*c*-3*e* bond to form [11]. Clark has proposed a general empirical equation which, in part, uses the IEs to predict the 2*c*-3*e* bond dissociation energy [12]. Based on this equation, the strongest 2*c*-3*e* bond is expected to occur between species of the same IE.

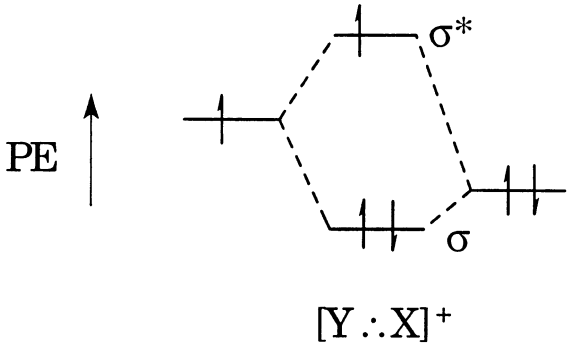

Scheme 2.

Furthermore, the overall stability of the 2*c*-3*e* bond does not vary linearly with orbital overlap. Instead, as orbital overlap becomes more positive, the destabilization of the σ^* antibonding orbital increases relative to the σ bonding orbital until no net bonding remains [13].

In studying the unsymmetric methyl halide systems, we hope not only to confirm the atomic connectivity of the mixed methyl halide association products, but to also learn more about the nature of unsymmetric 2*c*-3*e* bonding. In addition, by using the density functional theory (DFT) and phase space modeling, we hope to learn more about the fragmentation pathways and the potential energy surface (PES) for the systems studied.

2. Methods

2.1. Mass spectrometry

MS/MS experiments on the $[C_2H_6XY]^{\cdot +}$ association products were carried out with a modified VG-ZAB 1F [14,15]. Modifications include the addition of a collision cell in the second field-free region and the incorporation of a variable-temperature electron ionization/chemical ionization (EI/CI) ion source with a coaxial electron entrance/ion exit. The second field-free region collision cell was placed just before the β slit. MS/MS spectra were recorded using multiple scanning methods. Metastable scans were carried out in the second field-free region at a base pressure of 2×10^{-8} Torr. Kinetic energy release distributions (KERDs) were obtained from the metastable peaks shape by standard methods [16]. For collision-induced dissociation (CID) studies, helium was used as the collision gas with a peak attenuation of 40%.

All chemicals used in these experiments were commercially available. Samples were outgassed using several freeze–pump–thaw cycles and then dried on molecular sieves which had been baked out at temperatures slightly higher than 200 °C. The samples were transferred to, and stored in, glass bulbs which had been baked out by flaming with a torch under vacuum. Samples were introduced into the inlet line

via Granville–Phillips Series 203 leak valves and were allowed to mix in the inlet line.

Association cations were formed in the ion source as a result of ion/molecule reactions. An excess of the sample with the lowest IE was used in these experiments and the ratio of the pressures was varied in order to maximize signal. The CI slit was used and total source pressures were approximately 0.1 Torr. No bath gas was used. A source temperature of 400 K was maintained by passing air through stainless steel tubes silver-soldered to the source. Experiments were performed at electron energies of 70 eV.

2.2. Computational methods

2.2.1. DFT calculations

Calculations were performed using the GAUSSIAN 94 program system [17]. The geometry of each species was first optimized at the AM1 level and then used as the input for the DFT calculations at the B3LYP/6-31 + G(d,p) level of theory. The nature of the stationary points was checked by calculating vibrational frequencies. DFT calculations have been shown to often give a more accurate model of the energetics of reaction and bond dissociation than Hartree–Fock (HF) theory; hence, DFT was chosen for this study [18]. Density functionals have also been successful in reproducing known fundamental frequencies whereas HF, second-order Moller–Plesset (MP2), and quadratic configuration interaction calculation including single and double substitutions (QCISD) results are systematically too large [19]. Furthermore, spin contamination does not seem to be as serious for DFT as compared to HF theory [20].

In accordance with our previous methyl halide studies [2], a quasirelativistic effective core potential developed by Bergner et al. was used for the core electrons of bromine and iodine while the valence electrons were described with a 311/311/1 basis set contraction [21]. Using a pseudopotential simulates the effects of the core shells while restricting quantum chemical treatment to the valence shell. The basis set contraction was obtained by adding an additional s primitive and d primitive to the set proposed by Bergner. The additional s primitives are even tempered exponents of 0.056 for Br and 0.05 for I. A d exponent of 0.3 for I was arrived at by averaging the two d exponents from Dolg's larger valence set [22] which was found to be reliable by a previous study [2]. An additional d exponent of 0.35 was used for the bromine atom to account for the smaller atomic radius.

All association adducts were found to be stable minima containing 2c-3e bonds and were consistent with the experimental results. Although structures containing electrostatic interactions might be expected to give experimental results similar to those expected for the 2c-3e bonded adducts, this study focused on the 2c-3e bonded adducts found by DFT. As this was a combined experimental and theoretical study, the computational work focused on the experimental results and an exhaustive theoretical study of all possible structures was not undertaken.

2.2.2. Unimolecular kinetic modeling

Statistical phase space theory was used in modeling the KERDs for each system studied. The ability to model the experimental KERDs allows us to examine the PES for each system in more detail. Bowers and co-workers developed and supplied the phase space programs which were used to describe systems with competing fragmentation pathways and to calculate the corresponding kinetic energy releases [23]. The programs rigorously conserve energy and angular momentum [24]. Parameters such as rotational constants, vibrational frequencies, and energies used in the phase space calculations were taken from the optimized DFT results. Collision complex energies and angular momentum distributions are determined by thermal ion/molecule collisions [25]. Polarizabilities were taken from the literature [26].

The phase space calculations were carried out using the experimental temperature of 400 K and the calculated parameters for both the 2c-3e bonded association adducts and the loose orbiting transition states. The molecular parameters used for the phase space modeling have been provided in Tables 3–7 in the Appendix. Adjusting the adduct bond energies in order to fit the experimentally measured KERDs [24] did not have a large effect on the modeled KERs for these systems; therefore, the modeling used only the optimized DFT values.

Table 1
Total energies (hartrees), zero-point energies (kcal/mol)

Species	PG[a]	State	B3LYP/6-31+G*[b]	ZPE[c]
$CH_3I^{\cdot +}$	C_s	$2_{A'}$	−50.931 21	21.01
$CH_3Br^{\cdot +}$	C_s	$2_{A'}$	−52.912 88	20.82
$CH_3Cl^{\cdot +}$	C_s	$2_{A'}$	−499.697 31	20.60
$CH_3F^{\cdot +}$	C_1	2_A	−139.288 34	20.71
CH_3Br	C_{3v}	1_{A_1}	−53.301 19	23.33
CH_3Cl	C_{3v}	1_{A_1}	−500.111 52	23.87
CH_3F	C_{3v}	1_{A_1}	−139.751 08	24.72
$CH_2ClH^{\cdot +}$	C_1	2_A	−499.668 20	19.88
$[CH_3I\cdot\cdot BrCH_3]^{\cdot +}$	C_1	2_A	−104.200 06	46.80
$[CH_3I\cdot\cdot ClCH_3]^{\cdot +}$	C_1	2_A	−551.000 48	47.18
$[CH_3I\cdot\cdot FCH_3]^{\cdot +}$	C_1	2_A	−190.632 23	47.99
$[CH_3Br\cdot\cdot ClCH_3]^{\cdot +}$	C_1	2_A	−553.070 25	47.36
$[CH_3Br\cdot\cdot FCH_3]^{\cdot +}$	C_1	2_A	−192.619 07	48.07
$[CH_3IBr]^+$	C_1	2_A	−64.343 69	23.66
$[CH_3BrI]^+$	C_1	2_A	−64.339 25	23.87
$[CH_3BrCl]^+$	C_1	2_A	−513.121 35	24.10
$[CH_3ClBr]^+$	C_1	2_A	−513.118 27	24.41
$[CH_2ClH\text{-}FCH_3]^{\cdot +}$	C_s	$2_{A'}$	−639.473 13	27.31
$CH_3^{\cdot}$	D_{3h}	$2_{A_2''}$	−39.842 03	18.69

[a]Point group.
[b]I and Br calculations included the effective core potential from [21] and [22] and used a 311/311/1 basis set contraction basis set.
[c]Zero-point energy (kcal/mol), the number of imaginary frequencies was zero in all cases.

3. Results and discussion

MS/MS unimolecular and CID experiments yield information on the PES of the observed association products and their atomic connectivity. Metastable ions have low internal energies resulting in longer lifetimes than CID fragmenting ions [27,28]. These longer lifetimes allow for structural rearrangements which provide information on competing fragmentation pathways. CID fragmenting ions are short-lived due to their higher internal energies and do not usually undergo extensive rearrangement [29]. For this reason, CID spectra are more informative than metastable spectra in deducing the structures of ions and can provide more direct evidence of the atomic connectivity of ions [29]. Here, metastable ion reactions, CID, DFT calculations and phase space modeling have been used to further elucidate the structures and PESs for the ions studied.

Detailed DFT computational energies for the $[CH_3X\cdot\cdot YCH_3]^{\cdot +}$ systems are given in Table 1 and the geometries of the minimum energy association products are shown in Fig. 1. The PES used in the unimolecular kinetic modeling studies involved the halide radical cations and neutral halides reacting to form the $[CH_3X\cdot\cdot YCH_3]^{\cdot +}$ association adduct. The adducts undergo direct fragmentation to reform the reactants. No tight transition states or reverse activation barriers were employed.

3.1. $[CH_3I\cdot\cdot{}^{81}BrCH_3]^{\cdot +}$ and $[CH_3{}^{79}Br\cdot\cdot{}^{35}ClCH_3]^{\cdot +}$

The results on the $[CH_3I\cdot\cdot BrCH_3]^{\cdot +}$ system are given in Figs. 2–4. Two competing reactions were observed for the metastable decomposition of $[CH_3I\cdot\cdot BrCH_3]^{\cdot +}$, $m/z = 236$ (Fig. 2)

$$[CH_3I\cdot\cdot BrCH_3]^{\cdot +} \rightarrow CH_3I^{\cdot +} + CH_3Br \quad (1)$$

$$[CH_3I\cdot\cdot BrCH_3]^{\cdot +} \rightarrow CH_3IBr^+ + CH_3^{\cdot} \quad (2)$$

The most intense peak in the metastable product spectrum is due to formation of $CH_3I^{\cdot +}$, $m/z = 142$, which results from direct cleavage of the $2c$-$3e$ bond [reaction (1)]. CH_3I has a lower ionization energy than CH_3Br (9.54 and 10.54 eV, respectively) [30] and carries the charge as the two moieties separate.

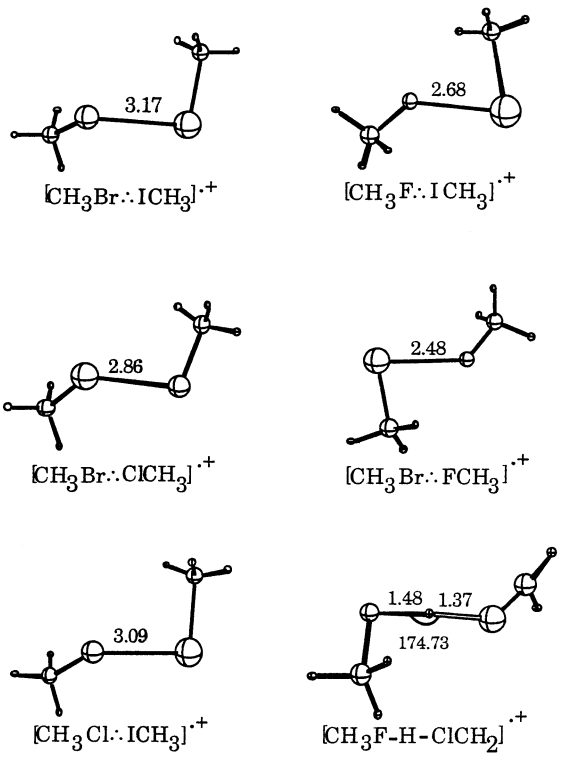

Fig. 1. DFT optimized minimum energy structures for all association adducts. Bond lengths are in angstroms.

DFT calculations indicate that reaction (2) is endothermic by 27.3 kcal/mol, therefore, CH_3IBr^+, $m/z = 221$ is believed not to originate from the $[CH_3I{\cdot}{\cdot}BrCH_3]^{\cdot +}$ ground state. The CH_3IBr^+ metastable product may result from a different parent isomer, an electronically excited state, or background CID. However, the large difference between the metastable spectra (Fig. 2) and the CID spectra (Fig. 3) strongly suggest that CH_3IBr^+ does not originate from background CID. Furthermore, we did not consider the existence of additional structures, $[(CH_3)_2I–Br]^+$, for example, that may provide a less endothermic pathway to the formation of CH_3IBr^+.

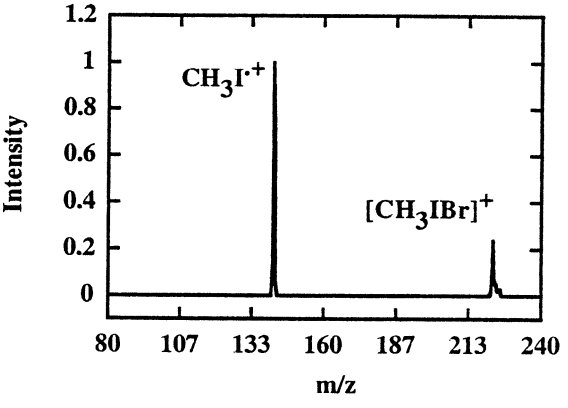

Fig. 2. MS/MS metastable spectrum of $[CH_3I{\cdot}{\cdot}{}^{81}BrCH_3]^{\cdot +}$.

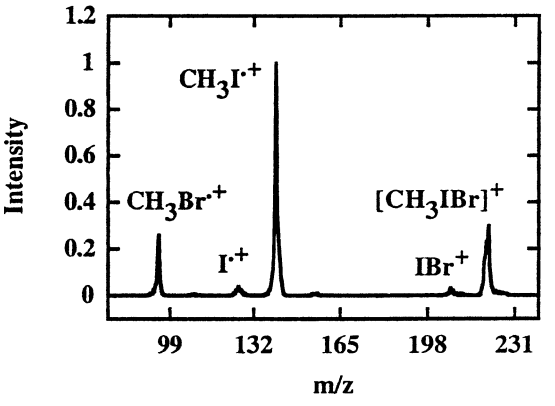

Fig. 3. Collision induced dissociation spectrum of $[CH_3I{\cdot}{\cdot}{}^{81}BrCH_3]^{\cdot +}$.

The KERD obtained from the metastable peak resulting from the direct cleavage of the 2*c*-3*e* bond in $[CH_3I{\cdot}{\cdot}BrCH_3]^{\cdot +}$ is shown in Fig. 4. The KERD

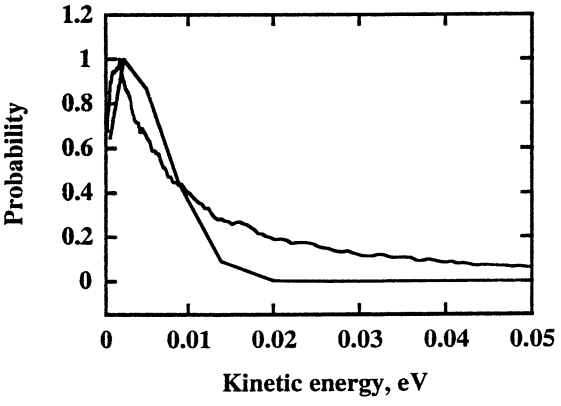

Fig. 4. Metastable kinetic energy release distributions and kinetic modeling results for $[CH_3I{\cdot}{\cdot}BrCH_3]^{\cdot +} \rightarrow CH_3I^{\cdot +} + CH_3Br$ (reaction 1). Phase space distributions are indicated by the solid continuous line.

results in an average KER of 7.3 meV. Fig. 4 also shows a reasonable agreement between experimental measurements and phase space calculations for the proposed fragmentation path. The ability to model the KERD with orbiting transition states resembling loosely associated products provides strong evidence that this process is a simple cleavage involving essentially no reverse activation barrier.

The KERD for reaction (2) was also measured experimentally; however, phase space calculations have not been performed. The experimental KERD is much broader than the KERD for the direct fragmentation reaction. The experimental average KER for CH_3IBr^+ is 102.9 meV. The broader KERD suggests that this process is more complicated than a simple direct fragmentation reaction and could originate from an electronically excited state since the energy partitioned into relative translational energy of the products will be greater if the products are formed from excited state ions [23].

The CID results for $[CH_3I.\cdot.BrCH_3]^{\cdot+}$ are given in Fig. 3. Two peaks arising from the direct cleavage of the 2*c*-3*e* bond, $CH_3I^{\cdot+}$, $m/z = 142$ and $CH_3Br^{\cdot+}$, $m/z = 96$ are observed. As expected from the IEs, the most intense peak in this spectrum is $CH_3I^{\cdot+}$. CH_3IBr^+, $m/z = 223$; I^+, $m/z = 127$ and $IBr^{\cdot+}$, $m/z = 208$ are also present in the CID spectrum. The latter two peaks are much less intense due to the greater number of bonds being broken. The presence of the weak $IBr^{\cdot+}$ and the stronger CH_3IBr^+ peaks in the CID spectrum provide support of the I–Br atomic connectivity in the $[CH_3I.\cdot.BrCH_3]^{\cdot+}$ radical cation.

The results on the $[CH_3Br.\cdot.ClCH_3]^{\cdot+}$ system given in Figs. 5–7 are similar to those just presented. The metastable spectra studied for $[CH_3Br.\cdot.ClCH_3]^{\cdot+}$, $m/z = 144$ (Fig. 5) shows two peaks believed to result from the following two reactions:

$$[CH_3Br.\cdot.ClCH_3]^{\cdot+} \rightarrow CH_3Br^{\cdot+} + CH_3Cl \quad (3)$$

$$[CH_3Br.\cdot.ClCH_3]^{\cdot+} \rightarrow CH_3ClBr^+ + CH_3^{\cdot} \quad (4)$$

An intense peak belonging to $CH_3Br^{\cdot+}$, $m/z = 94$ is observed for the direct cleavage of the 2*c*-3*e* bond while a much weaker peak, CH_3ClBr^+, $m/z = 129$ most likely does not result from the ground electronic

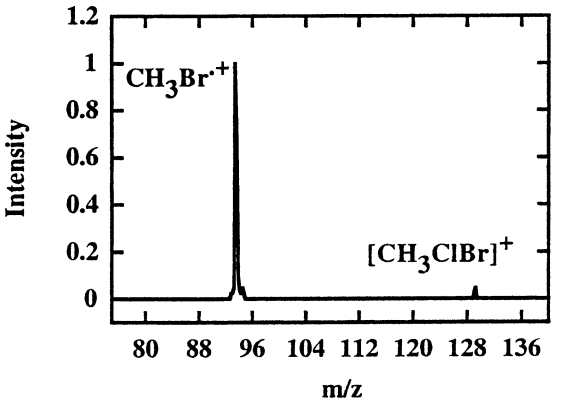

Fig. 5. MS/MS metastable spectrum of $[CH_3Br.\cdot.^{35}ClCH_3]^{\cdot+}$.

state since DFT calculations indicate that reaction (4) is endothermic by 36.4 kcal/mol. This product may result from a different parent isomer, an electronically excited state, or background CID, as noted in the previous discussion.

The KERD, obtained from the metastable peak arising from the direct cleavage of the 2*c*-3*e* bond in $[CH_3Br.\cdot.ClCH_3]^{\cdot+}$ is shown in Fig. 6, and results in an average KER of 7.4 meV. Phase space modeling using an orbiting transition state resembling loosely associated products indicates good agreement with experimental measurements. The ability to model the data with this type surface provides strong evidence

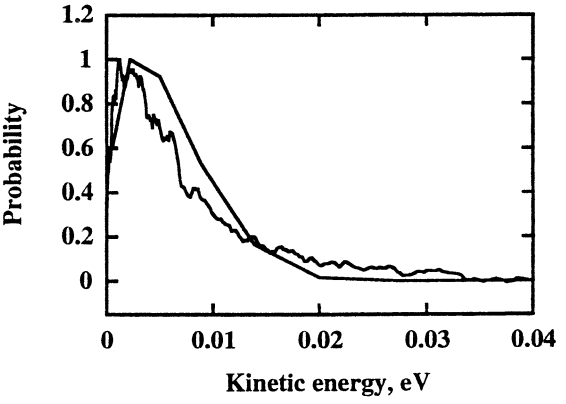

Fig. 6. Metastable kinetic energy release distributions and kinetic modeling results for $[CH_3Br.\cdot.ClCH_3]^{\cdot+} \rightarrow CH_3Br^{\cdot+} + CH_3Cl$ (reaction 3). Phase space results are represented by the solid continuous line.

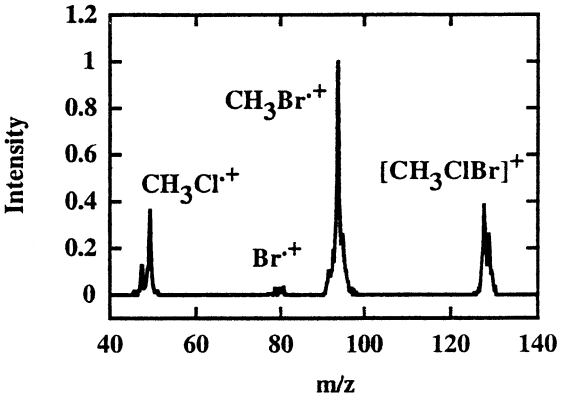

Fig. 7. Collision induced dissociation spectrum of $[CH_3Br\cdot\cdot\cdot{}^{35}ClCH_3]^{\cdot+}$.

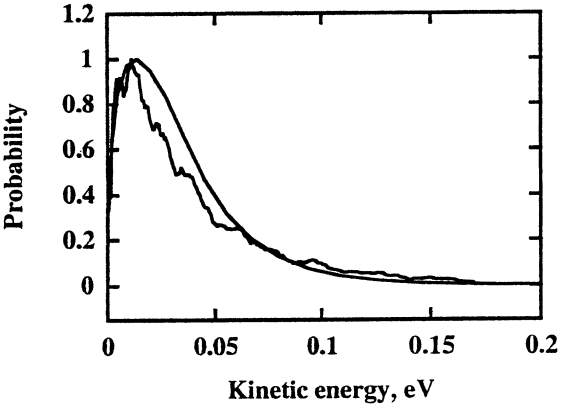

Fig. 8. Metastable kinetic energy release distribution and kinetic modeling results for $[CH_3I\cdot\cdot\cdot ClCH_3]^{\cdot+} \rightarrow CH_3I^{\cdot+} + CH_3Cl$ (reaction 5). Phase space results are indicated by the solid continuous line.

that this process is a simple cleavage involving essentially no reverse activation barrier.

The KERD for reaction (4) was also measured experimentally; however, as with reaction (2) in the above study, phase space calculations were not performed. The experimental average KER for CH_3IBr^+ is 102.9 meV and the KERD is much broader than the KERD for the direct fragmentation reaction. As with the $[CH_3I\cdot\cdot\cdot BrCH_3]^{\cdot+}$ system, the broader KERD suggests that reaction (4) is more complicated than a simple direct fragmentation.

The CID spectrum for $[CH_3Br\cdot\cdot\cdot ClCH_3]^{\cdot+}$ is given in Fig. 7. The most intense peak in this spectrum is $CH_3Br^{\cdot+}$, $m/z = 94$. $CH_3Cl^{\cdot+}$, $m/z = 50$, is also present in the spectrum. Both these ions result from cleavage of the same bond; the lower intensity of $CH_3Cl^{\cdot+}$ versus $CH_3Br^{\cdot+}$ is expected due to the higher IE of CH_3Cl. The only other major peak in the spectrum is CH_3ClBr^+, $m/z = 133$ which results from the loss of a methyl group and lends additional support to the Br–Cl atomic connectivity.

3.2. $[CH_3I\cdot\cdot\cdot{}^{35}ClCH_3]^{\cdot+}$, $[CH_3I\cdot\cdot\cdot FCH_3]^{\cdot+}$, and $[CH_3{}^{79}Br\cdot\cdot\cdot FCH_3]^{\cdot+}$

The results of the $[CH_3I\cdot\cdot\cdot{}^{35}ClCH_3]^{\cdot+}$, $[CH_3I\cdot\cdot\cdot FCH_3]^{\cdot+}$, and $[CH_3{}^{79}Br\cdot\cdot\cdot FCH_3]^{\cdot+}$ studies are given in Figs. 8–13. The metastable spectra for these three ions have only peaks due to direct fragmentation of the $2c$-$3e$ bond with retention of the charge on the moiety with the lowest IE, reactions (5)–(7)

$$[CH_3I\cdot\cdot\cdot ClCH_3]^{\cdot+} \rightarrow CH_3I^{\cdot+} + CH_3Cl \quad (5)$$

$$[CH_3I\cdot\cdot\cdot FCH_3]^{\cdot+} \rightarrow CH_3I^{\cdot+} + CH_3F \quad (6)$$

$$[CH_3Br\cdot\cdot\cdot FCH_3]^{\cdot+} \rightarrow CH_3Br^{\cdot+} + CH_3F \quad (7)$$

Figs. 8–10 show measured and calculated KERDs for these reactions. The average experimental KERs are 32.61, 116.0, and 77.6 meV, respectively. The aver-

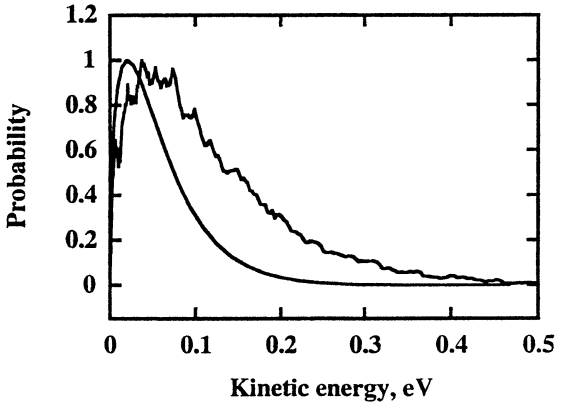

Fig. 9. Metastable kinetic energy release distribution and kinetic modeling results for $[CH_3I\cdot\cdot\cdot FCH_3]^{\cdot+} \rightarrow CH_3I^{\cdot+} + CH_3F$ (reaction 6). Phase space results are indicated by the solid continuous line.

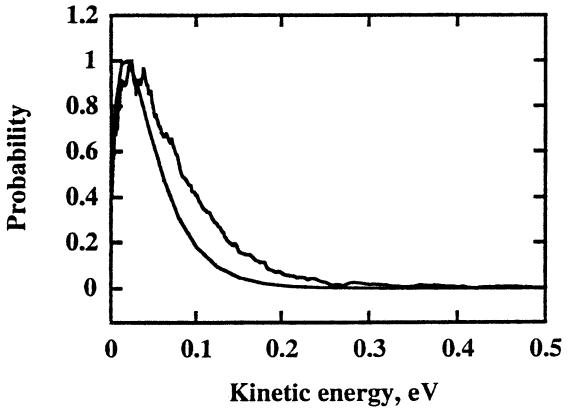

Fig. 10. Metastable kinetic energy release distribution and kinetic modeling results for $[CH_3Br.\therefore FCH_3]^{\cdot +} \rightarrow CH_3Br^{\cdot +} + CH_3F$ (reaction 7). Phase space results are indicated by the solid continuous line.

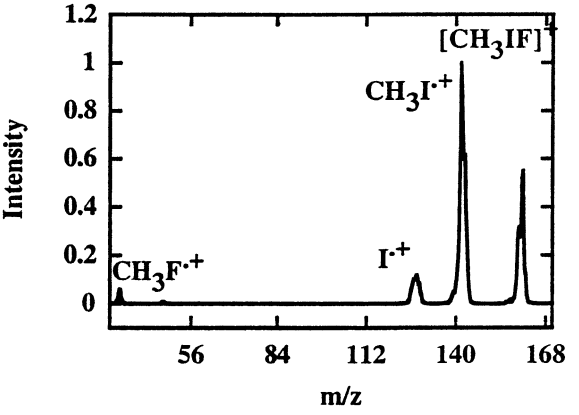

Fig. 12. Collision induced dissociation spectrum of $[CH_3I.\therefore FCH_3]^{\cdot +}$.

age KER increases as the X.∴Y bond energy (from the DFT calculations) decreases; this trend is discussed further in Sec. 3.3.

Orbiting transition states were used in the phase space modeling of the three metastable reactions (curves in Figs. 8–10). The orbiting transition states resemble loosely associated products and imply direct fragmentation. The fit between phase-space modeling and experiment (discussed further in Sec. 3.3) is not very good for reaction (6).

The CID spectra of $[CH_3I.\therefore ClCH_3]^{\cdot +}$, $[CH_3I.\therefore FCH_3]^{\cdot +}$, and $[CH_3Br.\therefore FCH_3]^{\cdot +}$ are shown in Figs. 11–13. One simple presentation of all three ions shows the most intense peak as the species with the lower IE which results from direct cleavage of the $2c$-$3e$ bond. The other peaks arising from this bond cleavage are much less intense due to the higher IEs of their respective neutrals. CH_3ICl^+, $m/z = 177$, CH_3IF^+, $m/z = 161$, and CH_3BrF^+, $m/z = 113$, resulting from the loss of a methyl group from the $[CH_3X.\therefore YCH_3]^{\cdot +}$ association adducts, are also seen in the CID spectra. These peaks imply a halogen–halogen connectivity in the adduct. The only other peaks present in this spectra, I^+, $m/z = 127$ and Br^+, $m/z = 79$ are much less intense as their formation requires breaking more than one bond.

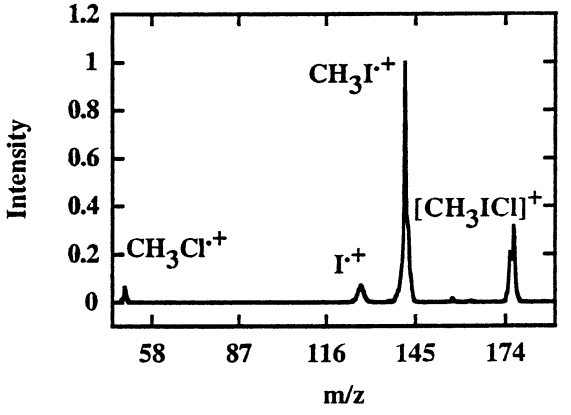

Fig. 11. Collision induced dissociation spectrum of $[CH_3I.\therefore {}^{35}ClCH_3]^{\cdot +}$.

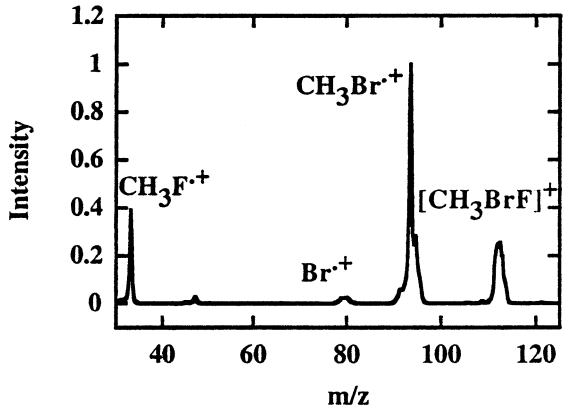

Fig. 13. Collision induced dissociation spectrum of $[CH_3Br.\therefore FCH_3]^{\cdot +}$.

Table 2
Calculated relative energies,[a] differences in IEs,[b] and experimental average KERs for direct cleavage of the 2*c*-3*e* bond

Species	Average KER (meV)	Energies (eV)	ΔIE (eV)
$[CH_3Br.\cdot.ClCH_3]^{\cdot+}$	7.4	−1.13	0.68
$[CH_3I.\cdot.BrCH_3]^{\cdot+}$	7.3	−1.04	1
$[CH_3I.\cdot.ClCH_3]^{\cdot+}$	32.6	−0.80	1.68
$[CH_3Br.\cdot.FCH_3]^{\cdot+}$	77.6	−0.75	1.93
$[CH_3I.\cdot.FCH_3]^{\cdot+}$	116.0	−0.62	2.93

[a]Zero-point energy corrections have been included.
[b]IEs were obtained from [30].

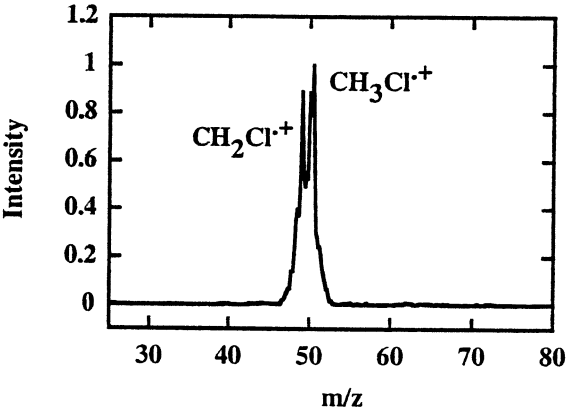

Fig. 14. Collision induced dissociation spectrum of $[C_2H_6FCl]^{\cdot+}$.

3.3. KERD trends

Table 2 gives the calculated bond energies, ΔIEs [30], and experimental average KERs for the direct fragmentation of the 2*c*-3*e* bond for all systems. It shows that as the 2*c*-3*e* bond energy increases, the difference in IEs of the two interacting moieties decreases and the average KER becomes smaller. As has already been noted, the strongest 2*c*-3*e* bond should occur between species with the same IE. Therefore, as demonstrated by these results, the 2*c*-3*e* bond strength has an inverse correlation with the ΔIE. The trend in the KERs arises from the fact that all ions start with a thermal energy distribution; hence, the adducts with the weakest bonds have the highest ratio of internal energy to energy required for bond cleavage.

$[CH_3I.\cdot.ClCH_3]^{\cdot+}$ and $[CH_3Br.\cdot.FCH_3]^{\cdot+}$ have only a small difference in bond energy while a large difference occurs in the average KER upon cleavage of the 2*c*-3*e* bond. This large difference in the average KER of the two ions scales with the polarizability difference between the neutral leaving groups (CH_3Cl = 5.35 Å^3 and CH_3F = 2.97 Å^3). The decrease in average KER with increasing polarizability has been previously noted and is consistent with computational results [31]. This effect is also seen in comparing the average KER for cleavage of $[CH_3I.\cdot.ClCH_3]^{\cdot+}$ with that of $[CH_3I.\cdot.FCH_3]^{\cdot+}$.

Reasons for the inability to correctly fit the measured KERD for the metastable $CH_3I^{\cdot+}$ product resulting from reaction (6) with the phase space modeling include the existence of an excited state or alternate structure at m/z = 176. Since the phase space calculations considered only the 2*c*-3*e* bonded association adduct, it is possible that, by considering other structures for this association adduct, a better fit might be obtained.

3.4. $[C_2H_6{}^{35}ClF]^{\cdot+}$

The observations on $[C_2H_6ClF]^{\cdot+}$ were very different than those for the ions already presented. No evidence for 2*c*-3*e* bonds resulted. Due to the low intensity of the main beam, we were unable to collect a metastable spectrum and only the CID spectrum for $[C_2H_6ClF]^{\cdot+}$ (Fig. 14) will be discussed. The peaks observed in this spectrum are $CH_2Cl^{\cdot+}$, m/z = 49 and $CH_3Cl^{\cdot+}$, or $CH_2ClH^{\cdot+}$, m/z = 50. Although m/z = 50 is consistent with the presence of a 2*c*-3*e* bond, the presence of $CH_2Cl^{\cdot+}$ in the CID spectra contradicts a 2*c*-3*e* bonded structure for $[C_2H_6ClF]^{\cdot+}$. Based on the CID spectrum, it is likely that $[C_2H_6ClF]^{\cdot+}$ has a H–F connectivity, $[CH_2Cl–H–FCH_3]^{\cdot+}$. Fragmentation of the Cl–H bond in this species would result in CH_2Cl^+ while breaking the H–F bond would result in $CH_3Cl^{\cdot+}$, or $CH_2ClH^{\cdot+}$ at m/z = 50.

Even though both isomers, the H–F bonded adduct and the 2*c*-3*e* bonded adduct, may be present; the structure most consistent with the experimental evidence, $[CH_2ClH–FCH_3]^{\cdot+}$, was studied using DFT and found to be a stable association adduct with a H–F

bond energy of 33.20 kcal. The calculated structure is shown in Fig. 1. This Cl–H–F atomic connectivity is similar to that in $[CH_2ClH–ClCH_3]^{\cdot +}$, a stable association adduct found in previous studies on $[C_2H_6Cl_2]^{\cdot +}$ [1,2].

4. Conclusions

Both the experimental and computational results support the presence of a 2*c*-3*e* bond for $[CH_3I{\cdot}{\cdot}BrCH_3]^{\cdot +}$, $[CH_3I{\cdot}{\cdot}ClCH_3]^{\cdot +}$, $[CH_3I{\cdot}{\cdot}FCH_3]^{\cdot +}$, $[CH_3Br{\cdot}{\cdot}ClCH_3]^{\cdot +}$, and $[CH_3Br{\cdot}{\cdot}FCH_3]^{\cdot +}$. All five ions show direct fragmentation of the 2*c*-3*e* bond. The average KER for the unimolecular fragmentations increases with decreasing 2*c*-3*e* bond energies as calculated using DFT. For ions with similar bond energies but different leaving groups, the average KER decreases with increasing polarizability of the neutral leaving group. Computational studies provide evidence of the 2*c*-3*e* bonded structure while the modeled KER for direct cleavage of the 2*c*-3*e* bond is consistent with statistical unimolecular decomposition which proceeds through an orbiting transition state. $[CH_3I{\cdot}{\cdot}BrCH_3]^{\cdot +}$ and $[CH_3Br{\cdot}{\cdot}ClCH_3]^{\cdot +}$ have a competing metastable fragmentation pathway resulting in formation of $[CH_3XY]^+$. The larger average KERs for this path and their large endothermic requirements indicate that the products formed most likely do not stem from the ground $[CH_3X{\cdot}{\cdot}YCH_3]^{\cdot +}$ electronic state.

The MS/MS CID experiments support the 2*c*-3*e* bonded structures, and all strong metastable pathways were successfully modeled using these structures. However, modeling of the weak $[CH_3I{\cdot}{\cdot}FCH_3]^{\cdot +}$ metastable proved to be problematic. Additional structures, excited states, and background CID are all plausible reasons for the inability to fit the experimental data.

The MS/MS CID experiments for the $[C_2H_6ClF]^{\cdot +}$ radical cations do not indicate the presence of a 2*c*-3*e* bond; instead, they give evidence of a different atomic connectivity, $[CH_2Cl–H–FCH_3]^{\cdot +}$. Computational work indicates this is a stable association product with similar atomic connectivity to that previously noted in $[C_2H_6F_2]^{\cdot +}$ studies [2].

Acknowledgements

One of the authors (A.J.I.) would like to acknowledge BASF for the donation of the ZAB 1F (serial No. 120). The authors are grateful to the Alabama Supercomputer Network for computer time and to David Young for his help with the DFT pseudopotential and phase space calculations. Another author (L.S.N.) is thankful to the USDE for a Graduate Assistance in Area of National Needs (GAANN) Fellowship. In addition, they would like to express their appreciation to Petra A. M. van Koppen and Michael T. Bowers (University of California, Santa Barbara) and Susan T. Graul (Carnegie Mellon) for their assistance with the phase space programs.

References

[1] S.P. de Visser, L.J. de Koning, N.M.M. Nibbering, J. Am. Chem. Soc. 120 (1998) 1517.
[2] L.S. Nichols, M.L. McKee, A.J. Illies, J. Am. Chem. Soc. 120 (1998) 1538.
[3] A.B. Hess Jr., R. Zahradnik, J. Am. Chem. Soc. 112 (1990) 5731.
[4] R. Zahradnik, Acc. Chem. Res. 28 (1995) 306.
[5] D.K. Maity, H. Mohan, Chem. Phys. Lett. 230 (1994) 351.
[6] K.-D. Asmus, H. Mohan, J. Phys. Chem. 92 (1988) 118.
[7] L.C.T. Shoute, P. Neta, J. Phys. Chem. 95 (1991) 4411.
[8] J.A. Booze, T. Baer, J. Chem. Phys. 96 (1992) 5541.
[9] A.J. Illies, P. Livant, J. Am. Chem. Soc. 113 (1991) 1510.
[10] L.J. Pauling, J. Am. Chem. Soc. 53 (1931) 3225.
[11] D.C. Young, M.L. McKee, Recent Trends in Computational Chemistry, Vol. 4, in press.
[12] T. Clark, J. Am. Chem. Soc. 110 (1988) 1672.
[13] K.-D. Asmus, J. Am. Chem. Soc. 12 (1979) 436.
[14] A.J. Illies, L.S. Nichols, M.A. James, J. Am. Soc. Mass Spectrom. 8 (1997) 605.
[15] M.A. James, M.L. McKee, A.J. Illies, J. Am. Chem. Soc. 118 (1996) 7836.
[16] M.F. Jarrold, A.J. Illies, N.J. Kirchner, W. Wagner-Redecker, M.T. Bowers, M.L. Maudich, J.L. Beauchamp, J. Phys. Chem. 87 (1983) 2213.
[17] M.J. Frisch, G.W. Trucks, H.B. Schlegel, P.M.W. Gill, B.G. Johnson, M.A. Robb, J.R. Checseman, T. Kieth, G.A. Petersson, J.A. Montgomery, K. Ragharachari, M.A. Allaham, V.G. Zakrzewski, J.V. Ortiz, J.B. Foresmar, J. Cioslowski, B.B. Stefanov, A. Nanayakkara, M. Challacombe, C.Y. Peng, P.V. Ayala, W. Chen, J. Martin, J.P. Stewart, M. Head-Gordon, C. Gonzalez, J.A. Pople, GAUSSIAN 94, revision B.1, Gaussian, Inc., Pittsburgh, PA, 1995.
[18] T. Ziegler, Chem. Rev. 91 (1991) 651.

[19] B.G. Johnson, P.M.W. Gill, J.A. Pople, J. Chem. Phys. 98 (1993) 5612.
[20] J. Baker, A. Scheiner, J. Andzelm, Chem. Phys. Lett. 216 (1993) 380.
[21] A. Bergner, M. Dolg, W. Kuchle, H. Stoll, H. Preuß, Mol. Phys. 80 (1993) 1431.
[22] M. Dolg, database at http://www.theochem.uni-stuttgart.de/
[23] C.J. Carpenter, P.A.M. Van Koppen, M.T. Bowers, J. Am. Chem. Soc. 117 (1995) 10976.
[24] M.A. Hanratty, J.L. Beauchamp, A.J. Illies, P. Van Koppen, M.T. Bowers, J. Am. Chem. Soc. 110 (1988) 1.
[25] L.M. Bass, R.D. Cates, M.F. Jarrold, N.J. Kirchner, M.T. Bowers, J. Am. Chem. Soc. 105 (1983) 7024.
[26] CRC Handbook of Chemistry and Physics: David R. Lide (Ed.), CRC, Boca Raton, FL, 1994.
[27] K.R. Jennings, Int. J. Mass Spectrom. Ion Phys. 1 (1968) 227.
[28] F.W. McLafferty, P.F. Bente III, R. Kornfeld, S.C. Tsai, I. Howe, J. Am. Chem. Soc. 95 (1973) 2120.
[29] R.G. Cooks, J.H. Beynon, R.M. Caprioli, G.R. Lester, Metastable Ions, Elsevier, Amsterdam, The Netherlands, 1973.
[30] S.G. Lias, J.E. Bartmess, J.F. Liebman, J.L. Holmes, R.D. Levin, W.G. Mallard, Journal of Physical and Chemical Reference Data: American Chemical Society and the American Institute of Physics for the National Bureau of Standards, 1988, vol. 17.
[31] A.J. Illies, M.F. Jarrold, L.M. Bass, M.T. Bowers, J. Am. Chem. Soc. 105 (1983) 5775.

Appendix

Table 3
Input parameters for phase space calculations on $[CH_3I^{\cdot}\cdot BrCH_3]^{\cdot +}$ system

Property	$CH_3I^{\cdot +}$	CH_3Br	$[CH_3I^{\cdot}\cdot BrCH_3]^{\cdot +}$
σ	1	3	1
α (Å^3)[a]		5.87	
B (cm^{-1})[b]	1.8489	1.9353	0.0662
ν (cm^{-1})[b]	430	587	31
	443	961	43
	944	962	62
	1237	1337	70
	1300	1479	70
	1422	1479	112
	3046	3096	475
	3060	3209	529
	3242	3209	915
			935
			954
			969
			1313
			1332
			1447
			1451
			1453
			1458
			3097
			3098
			3216
			3217
			3244
			3245

[a]Polarizabilities were taken from the literature [26].
[b]Rotational constants, and vibrational frequencies were taken from the DFT calculations.

Table 4
Input parameters for phase space calculations on $[CH_3Br\cdot\cdot ClCH_3]^{\cdot +}$ system

Property	$CH_3Br^{\cdot +}$	CH_3Cl	$[CH_3Br\cdot\cdot ClCH_3]^{\cdot +}$
σ	1	3	1
α (Å^3)[a]		5.35	
B (cm^{-1})[b]	1.8844	2.025	0.1025
ν (cm^{-1})[b]	413	715	25
	484	1044	62
	973	1044	72
	1207	1412	77
	1283	1503	85
	1407	1503	172
	2966	3093	515
	3009	3191	623
	3236	3191	942
			972
			1012
			1035
			1330
			1379
			1436
			1443
			1450
			1459
			3081
			3085
			3194
			3205
			3231
			3245

[a]Polarizabilities were taken from the literature [26].
[b]Rotational constants, and vibrational frequencies were taken from the DFT calculations.

Table 5
Input parameters for phase space calculations on $[CH_3I^{\cdot}.ClCH_3]^{\cdot+}$ system

Property	$CH_3I^{\cdot+}$	CH_3Cl	$[CH_3I^{\cdot}.ClCH_3]^{\cdot+}$
σ	1	3	1
α (Å^3)[a]		5.35	
B (cm^{-1})[b]	1.8489	2.025	0.0828
ν (cm^{-1})[b]	430	715	20
	443	1044	48
	944	1044	60
	1237	1412	76
	1300	1503	78
	1422	1503	146
	3046	3093	472
	3060	3191	635
	3242	3191	910
			936
			1020
			1036
			1312
			1382
			1441
			1450
			1455
			1465
			3090
			3092
			3202
			3211
			3229
			3244

[a]Polarizabilities were taken from the literature [26].
[b]Rotational constants, and vibrational frequencies were taken from the DFT calculations.

Table 6
Input parameters for phase space calculations on $[CH_3I^{\cdot}.FCH_3]^{\cdot+}$ system

Property	$CH_3I^{\cdot+}$	CH_3F	$[CH_3I^{\cdot}.FCH_3]^{\cdot+}$
σ	1	3	1
α (Å^3)[a]		2.97	
B (cm^{-1})[b]	1.8489	2.286	0.1080
ν (cm^{-1})[b]	430	715	20
	443	1044	39
	944	1044	65
	1237	1412	69
	1300	1503	101
	1422	1503	174
	3046	3093	462
	3060	3191	887
	3242	3191	902
			935
			1157
			1166

Table 6 *(continued)*

Property	$CH_3I^{\cdot+}$	CH_3F	$[CH_3I^{\cdot}.FCH_3]^{\cdot+}$
			1308
			1424
			1439
			1462
			1472
			1482
			3081
			3086
			3198
			3202
			3212
			3241

[a]Polarizabilities were taken from the literature [26].
[b]Rotational constants, and vibrational frequencies were taken from the DFT calculations.

Table 7
Input parameters for phase space calculations on $[CH_3Br^{\cdot}.FCH_3]^{\cdot+}$ system

Property	$CH_3Br^{\cdot+}$	CH_3F	$[CH_3Br^{\cdot}.FCH_3]^{\cdot+}$
σ	1	3	1
α (Å^3)[a]		2.97	
B (cm^{-1})[b]	1.8844	2.286	0.1367
ν (cm^{-1})[b]	413	715	17
	484	1044	44
	973	1044	74
	1207	1412	77
	1283	1503	118
	1407	1503	214
	2966	3093	503
	3009	3191	866
	3236	3191	918
			968
			1148
			1163
			1320
			1410
			1436
			1451
			1453
			1477
			3060
			3078
			3185
			3189
			3218
			3237

[a]Polarizabilities were taken from the literature [26].
[b]Rotational constants, and vibrational frequencies were taken from the DFT calculations.